Optics & Laser Technology 157 (2023) 108732

Contents lists available at ScienceDirect

Optics and Laser Technology

journal homepage: www.elsevier.com/locate/optlastec

Full length article

A study on developing process-structure–property relationship with molten pool thermal history during laser surface remelting of Inconel 718

Arkajyoti Jha [a], Shivam Shukla [a], Amit Choudhary [a,b], Ramji Manoharan [a], Gopinath Muvvala [a,*]

[a] Department of Mechanical and Aerospace Engineering, Indian Institute of Technology Hyderabad, India
[b] Department of Mechanical and Industrial Engineering, Indian Institute of Technology Roorkee, India

ARTICLE INFO

Keywords:
Laser surface remelting
Inconel 718
Cooling rate
Microstructure evolution
Process map

ABSTRACT

In the area of laser material processing, laser surface remelting has been found to be an effective method of improving surface properties such as hardness, wear, and corrosion resistance. However, the scale of improvement depends on the evolving microstructure and phases, which depend on the cooling rates. Therefore, in the present study, laser surface remelting of Inconel 718 was carried out and a process-structure–property relationship with respect to the cooling rates has been developed. During the laser surface remelting process, the molten pool thermal history i.e. cooling rate, molten pool lifetime, and solidification shelf time is monitored and estimated using an IR pyrometer. The evolution of microstructure is later correlated with these parameters. With an increase in scan speed, the cooling rate is found to increase resulting in transformation of microstructure from equiaxed grains to columnar epitaxial growth. Based on the results obtained, a process map is proposed to establish a particular type of microstructure with respect to the cooling rate. Further, the effect of cooling rate and microstructure on the surface hardness and specific wear rate has also been investigated. Both surface hardness and specific wear rate got reduced with decreasing cooling rate at a slower scan speed due to grain coarsening and an increase in elemental segregation or Laves phase formation.

1. Introduction

Inconel 718 is a nickel-based superalloy, and because of its superior high-temperature microstructural stability, it is widely used in the aerospace industry for making high-pressure turbine blades and components in the hot sections of rocket engines such as combustion chamber inlet, turbine and pre-burner exhaust [1,2]. With prolonged usage, these components are subjected to wear and tear. Owing to the high cost of material and manufacturing process, worn-out components are refurbished using laser-directed energy deposition or other additive manufacturing processes. However, the evolution of microstructure during the refurbishment process plays an important role in the resulting mechanical properties. To meet the increasing demand for output and to withstand the harsh high stress and corrosive environments at high temperatures, components like aero gas turbine blades are either made with directionally solidified or single-crystal superalloys [3], while the elements of a rocket are fabricated with polycrystalline structures [4]. Therefore, it becomes essential to enforce the parental microstructure in the areas of refurbishment. However, due to the slow cooling rate and constitutional supercooling, the microstructure at the surface exhibits stray grain or equiaxed structure [5,6], interrupting the epitaxial or columnar dendritic growth, commonly known as columnar to equiaxed transition (CET), which requires to be grinded or remelted [7]. Among these, remelting by high-energy beams like laser or electron beam was found to improve the surface properties like hardness, wear, and corrosion resistance by refining the microstructure [8,9]. Once again, it depends on the cooling rates involved [8,9]. Thus, it is necessary to understand the relation between the process parameters, molten pool thermal history (cooling rate), and the resulting microstructure.

Many researchers have focused on understanding the underlying mechanisms of CET or the microstructural evolution with respect to the cooling rate. Lei et al. [4] investigated microstructure evolution in multi-layered deposition. They reported the formation of stray grains as well as disorientated dendrites at the top surface as a function of temperature gradient and undercooling. Liang et al. [10] reported the loss of epitaxy and formation of stray grains due to the elemental segregation in the interdendritic region near the substrate surface favoring the formation of stray grains. Helmer et al. [11] studied the effect of scan strategy on producing either a columnar grain structure with a high texture along the building direction or an equiaxed fine-grained

* Corresponding author at: Department of Mechanical and Aerospace Engineering, IIT Hyderabad, Kandi, Sangareddy, Telangana 502285, India.
E-mail address: mgopinath@mae.iith.ac.in (G. Muvvala).

https://doi.org/10.1016/j.optlastec.2022.108732
Received 30 May 2022; Received in revised form 4 August 2022; Accepted 29 September 2022
Available online 11 October 2022

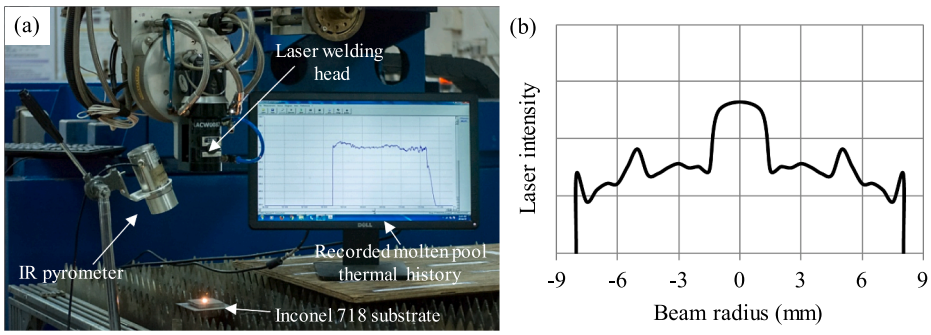

Fig. 1. Experimental setup used in the present study (a) overall setup, and (b) laser beam intensity profile [13].

Table 1
Process parameters.

Laser beam power	Scan speed	Spot diameter	Shielding gas
1200 W (10 l/min flow rate)	Varied from 200 mm/min to 1400 mm/min with an interval of 200 mm/min	3 mm	Argon

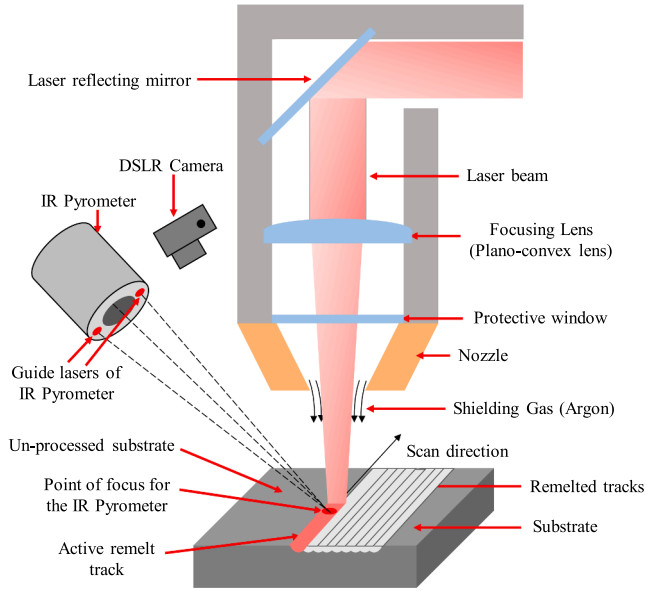

Fig. 2. Schematic of laser remelting with molten pool monitoring setup.

structure and the possibility of controlling them. Zhang et al. [12] investigated the effect of scan speed on the evolution of microstructure in laser remelting of Inconel 718 clad and reported its refinement with an increase in scan speed. This is attributed to the increase in the cooling rate with the scan speed, estimated based on the dendritic arm spacing. From the above studies, it is evident that the formation of columnar dendritic or directional solidification depends on the cooling rate which is a function of temperature gradient '*G*' (K/m) and solidification rate '*V*' (m/s).

Most of the existing studies focus on correlating the microstructural evolution after the deposition or remelting process with the available empirical relations to understand the cooling rates involved and correlating it with the process parameters. However, there exist no studies on quantifying the cooling rates during the deposition or remelting process. Further, optimization of the process with respect to process parameters may not guarantee its repeatability and reproducibility due to the influence of a large number of process parameters, many of which are system-dependent like the wavelength of the laser used, and its energy distribution, etc. Therefore, the present study primarily focuses on capturing the thermal history of the molten pool during the remelting process with the help of an IR pyrometer and development of the process–thermal history (cooling rate)-structure–property relationship. Further, the influence of process parameters on the geometrical aspects, hardness, and wear properties are also investigated and reported.

2. Experimental details

Fig. 1(a) shows the experimental setup used in the present study. A 2 kW Yb-fiber laser (IPG photonics, Model no. YLR 2000) is employed for the laser surface remelting of Inconel 718. The laser beam has an M^2 value close to 25 with a beam intensity profile having maximum intensity at the center and two annular rings of relatively low intensity as shown in Fig. 1(b) [13]. A 16 mm collimated laser beam is focused to 3 mm diameter over the substrate surface using a plano-convex lens of 200 mm focal length. Argon gas at 10 l/min flow rate is used to shield the molten pool from oxidation. Inconel 718 plates of 30 mm × 30 mm × 5 mm dimension are used as the substrate. Before remelting, grit blasting has been carried out on the substrate surface to increase the laser absorptivity and later cleaned in an ultrasonic bath with ethanol. Table 1 summarises the process parameters used in the present study.

The schematic of the experimental setup is shown in Fig. 2. An IR pyrometer (Make: Micro Epsilon, Model: CTLM-2HCF3–C3H) operating at 1.6 μm wavelength with an acquisition time, focal length, vision zone, accuracy, and temperature measurement range of 1 ms, 200 mm, 0.7 mm diameter, ± (0.3 % of reading + 2 °C) and 385–1600 °C, respectively has been employed to monitor the molten pool thermal history. To protect the pyrometer from back-reflected laser radiation, a 1064 ± 25 nm notch filter is mounted in front of the IR pyrometer and the pyrometer is recalibrated accordingly. The details of recalibration procedure is explained in detail in authors previous work [14]. During the remelting process, the substrate and pyrometer are kept stationary while the laser beam is moved linearly, scanning over the substrate. The pyrometer is always kept focused on a point that lies on the line of laser irradiation, using two diode guide lasers provided on the pyrometer. Further, the molten pool images are acquired using a digital single-lens reflex (DSLR) camera (Nikon D5200 mounted with 55–200 mm lens) with F-number (focal ratio) 36 and an exposure time of 1/4000 s set at an angle close to 80° with respect to the substrate surface. Further, a density-based clustering technique has been employed to convert the RGB images to a greyscale one, depicting isotherms qualitatively.

Single track experiments are carried out to investigate the effect of process parameters on bead geometry and molten pool thermal history, while surface remelting is executed with 30 % overlap between the tracks while performing the wear test. The remelted samples are sectioned using a wire-cut EDM, and the cross-sectioned part is then polished to a mirror-finish using SiC paper from P400 to P2000 grade,

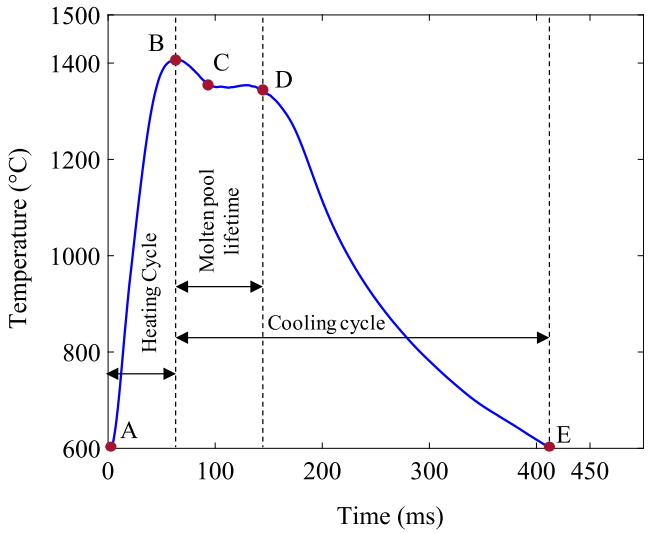

Fig. 3. Typical molten pool thermal cycle (1200 W, 1400 mm/min, 3 mm spot diameter).

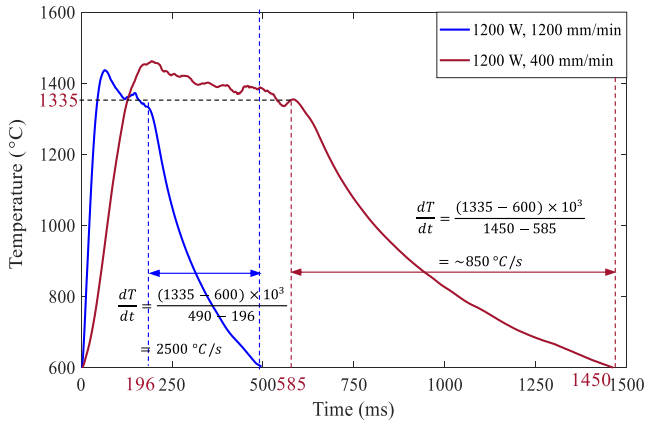

Fig. 4. Variation in molten pool thermal cycle and cooling rate with laser scan speed (3 mm spot diameter).

followed by 1 μm diamond paste. The samples are then etched in a solution comprising 10 mL acetic acid, 10 mL HNO_3, and 15 mL HCl by immersing them for about 20 s. The microstructural analysis is then carried out using a scanning electron microscope (Zeiss, EVO 18 Research), while the melt track geometry is analyzed and quantified using an optical microscope and ImageJ software, respectively. The wear test on the remelted samples is carried out using a ball-on-disk setup (Make: Ducom Instruments, TR-20LE-PHM-300) with a 10 mm diameter WC ball as counter body and 30 N load. The track diameter, rpm, and duration are set at 20 mm, 200 rpm, and 20 min, respectively, resulting in a 250 m sliding distance. The volume loss of the material is estimated by measuring the wear track profile using surface profilometer (MarSurf XT 20) at three different locations across the wear track followed by which the specific wear rate i.e. volume loss per-unit meter per unit load is calculated. Variation in the hardness along the melt depth is also measured using a Vickers hardness tester (Walter UHL, Model: VMH-001) kept at 50 g load with 15 s dwell time.

3. Results and discussion

3.1. Molten pool thermal history and its variation with process parameters

Fig. 3 shows a typical molten pool thermal history recorded using an IR pyrometer during the laser remelting of Inconel 718. As represented in Fig. 3, the molten pool thermal cycle consists of a heating cycle (*AB*) and cooling cycle (*BE*). As the laser beam irradiates on the substrate surface, its temperature rises rapidly above the melting point, reaching a peak temperature '*B*'. As the laser beam proceeds ahead, the molten pool behind the laser beam starts cooling down, exhibiting different phases. Initially, the molten pool temperature starts decreasing and reaches the liquidus temperature (point *C*), below which the solidification process initiates and ends at solidus temperature (point *D*). The zone *BC* and *CD* are termed as liquid state cooling and solidification shelf, respectively. The duration of the events *BD* and *CD* are called molten pool lifetime and solidification shelf time, respectively. The zone *DE* represents the solid phase cooling of the material.

Depending upon the process parameters, the thermal cycle profile and duration of each of these events in the cooling cycle vary, influencing the evolution of the microstructure [15]. Fig. 4 shows the variation in molten pool thermal cycle profile with the laser scan speed i.e., at 1200 mm/min and 400 mm/min. With the decrease in laser scan speed from 1200 mm/min to 400 mm/min, the line energy, i.e., energy input per unit length, defined as laser beam power divided by scan speed, increases from 60 J/mm to 180 J/mm. Further, the interaction time, defined as laser spot diameter divided by scan speed, increases from 150 ms to 450 ms. This increased line energy and interaction time increase the molten pool size, as shown in Fig. 5, and it can be observed that with a change in scan speed from 1200 mm/min to 200 mm/min, the molten pool size almost got doubled. This increase in the molten pool volume and decrease in temperature gradient due to longer interaction time results in a reduced cooling rate which is evident from Fig. 4. Further, Fig. 6 shows the variation in molten pool lifetime, solidification shelf time, and cooling rate with the scan speed. It is observed that with an increased scan speed, both molten pool lifetime and solidification shelf time get decreased. This is attributed to the decreasing molten pool size with a decrease in line energy, as well as due to an increased temperature gradient between the molten pool and the substrate, arising due to lower interaction time. This further increases the cooling rate

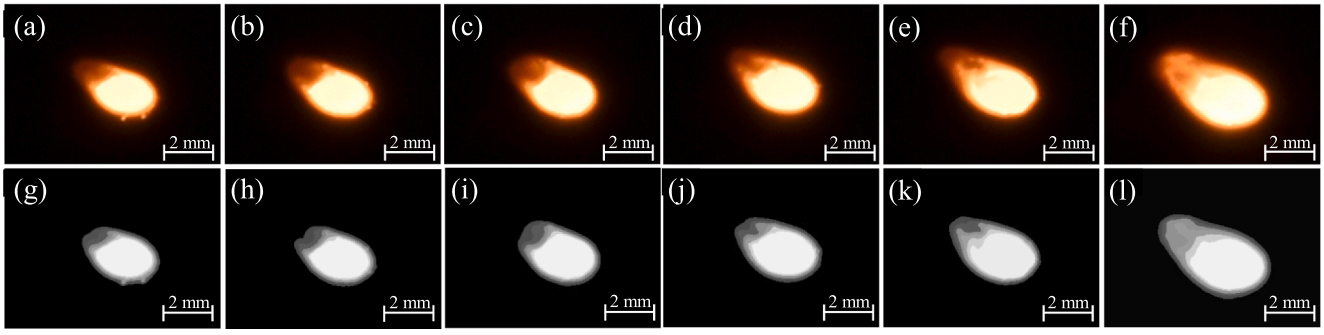

Fig. 5. Variation in molten pool size with laser scanning speed (a), (g) 1200 mm/min, (b), (h) 1000 mm/min, (c), (i) 800 mm/min, (d), (j) 600 mm/min, (e), (k) 400 mm/min and (f), (l) 200 mm/min (1200 W, 3 mm spot diameter).

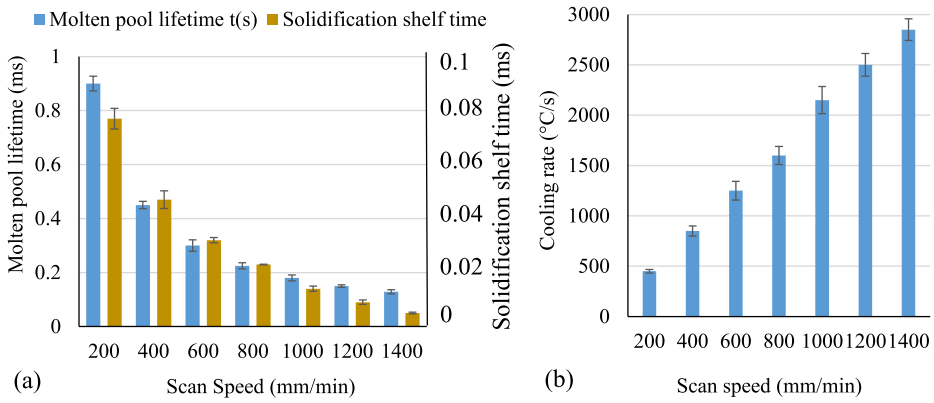

Fig. 6. Effect of laser scan speed on (a) molten pool lifetime and solidification shelf time and (b) cooling rate (1200 W, 3 mm spot diameter).

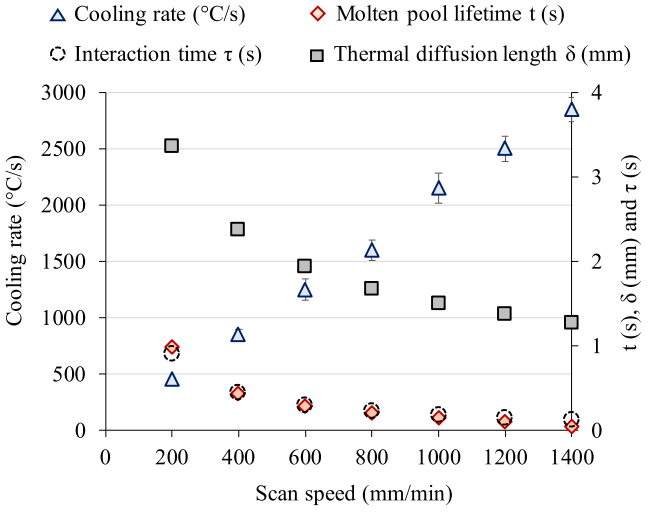

Fig. 7. Effect of laser scan speed on cooling rate (°C/s), molten pool lifetime t (s), interaction time τ (s), thermal diffusion length δ (mm) (1200 W, 3 mm spot diameter).

with respect to the scan speed, as shown in Fig. 6(b).

Fig. 7 shows the correlation between various aspects of molten pool thermal history, i.e., molten pool lifetime and cooling rates with respect to interaction time and thermal diffusion length calculated using Eq. 1, 2, and 3, where K is the thermal conductivity (11.1 W/m K), ρ is the density (8230 kg/m^3), C_p is the specific heat (435 J/kg K), D is the laser beam diameter, and V is the laser scan speed. It is observed that the molten pool lifetime and interaction time followed a similar trend with values close to each other. Further, as discussed, the thermal diffusion length decreased with an increase in the scan speed, thereby establishing a higher thermal gradient, resulting in an increased cooling rate.

$$\textit{Thermal diffusion length } \delta = 2\sqrt{\kappa\tau}$$

$$\textit{Thermal diffusivity } \kappa = \frac{K}{\rho C_p}$$

$$\textit{Interaction time } \tau = \frac{D}{V}$$

$$\lambda_S = \left(\frac{\alpha}{R_C}\right)^{-\beta}$$

It may be noted that the cooling rates derived experimentally from

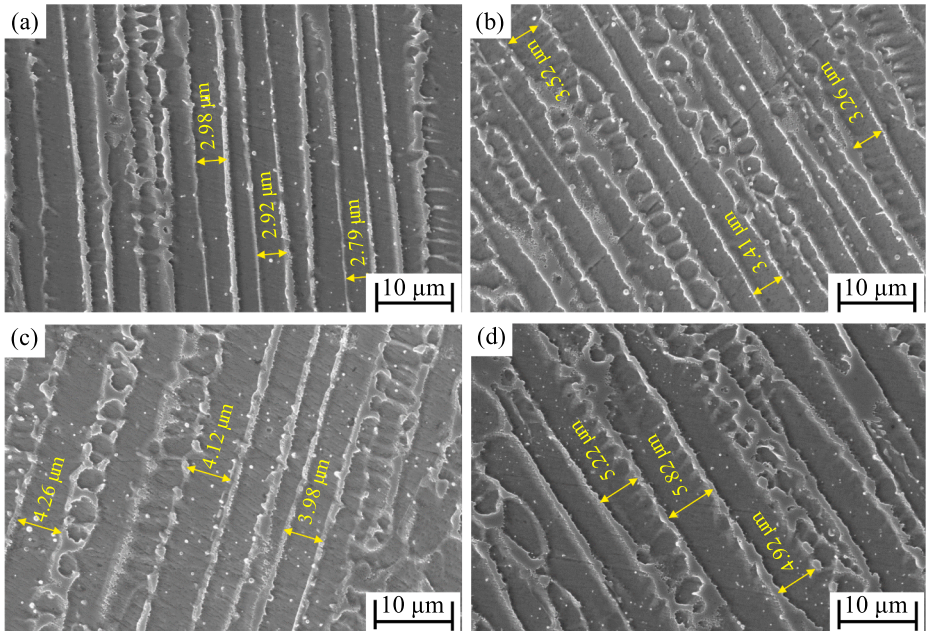

Fig. 8. Effect of scan speed on dendritic arm spacing (a) 1200 mm/min, (b) 800 mm/min, (c) 600 mm/min and (d) 200 mm/min (1200 W, 3 mm spot diameter).

Table 2
Values of α and β from the literature [16].

α	β	Equation	Reference
62.9	0.407	$R_C = (62.9/\lambda_S)^{1/0.407}$	[17]
31	1/3	$R_C = (31/\lambda_S)^3$	[18]
46.9	1/3	$R_C = (46.9/\lambda_S)^3$	[19]
65.9	1/3	$R_C = (65.9/\lambda_S)^3$	[20]

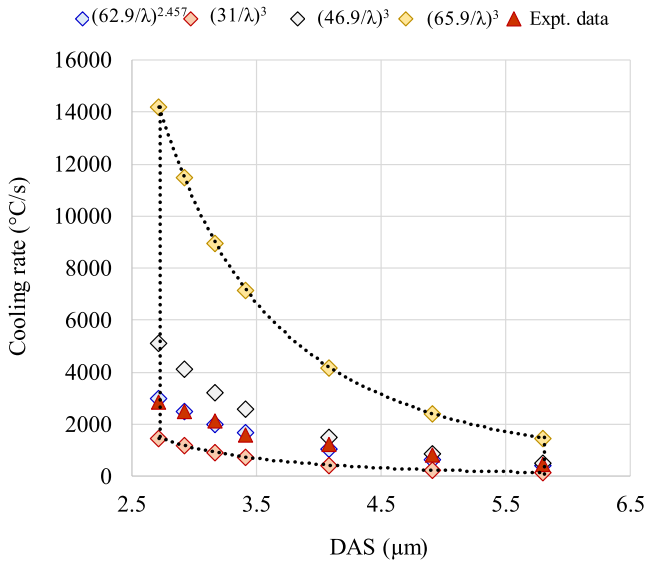

Fig. 9. Cooling rate vs dendritic arm spacing (DAS).

the molten pool thermal cycles, as shown in Fig. 4, are based on the temperature of the molten pool measured on the surface over a spot diameter of ~1 mm. To validate the cooling rates determined experimentally, based on the thermal cycles recorded using the IR pyrometer, a model fit has been established between the cooling rate (R_C) using the dendritic arm spacing (λ_S) as shown in Eq. 4. Here, α and β are constant parameters for a given alloy and solidification process-dependent coarsening parameters, respectively. The values of the dendritic arm spacing for the current set of experiments have been determined from the microstructural analysis of the laser remelted sample, analyzed using an SEM, as shown in Fig. 8. It is observed that with a decrease in scan speed, the dendritic arm spacing is found to increase due to an increase in the molten pool lifetime or solidification time, which signifies reduced cooling rates. Based on the λ_S values obtained from Fig. 8, the cooling rate is determined using Eq. 4 and then compared with the experimental results. The values of α and β are taken from the literature as shown in Table 2.

Fig. 9 shows the cooling rates calculated from the data in Table 2 and the dendritic spacing obtained from the experimental results. It can be observed that the experimental results agree very well with the results

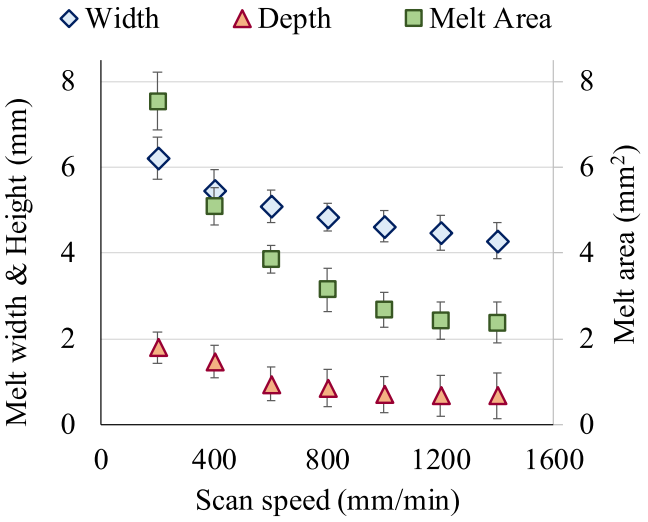

Fig. 11. Effect of laser scan speed on melt track width, depth, area (1200 W, 3 mm spot diameter).

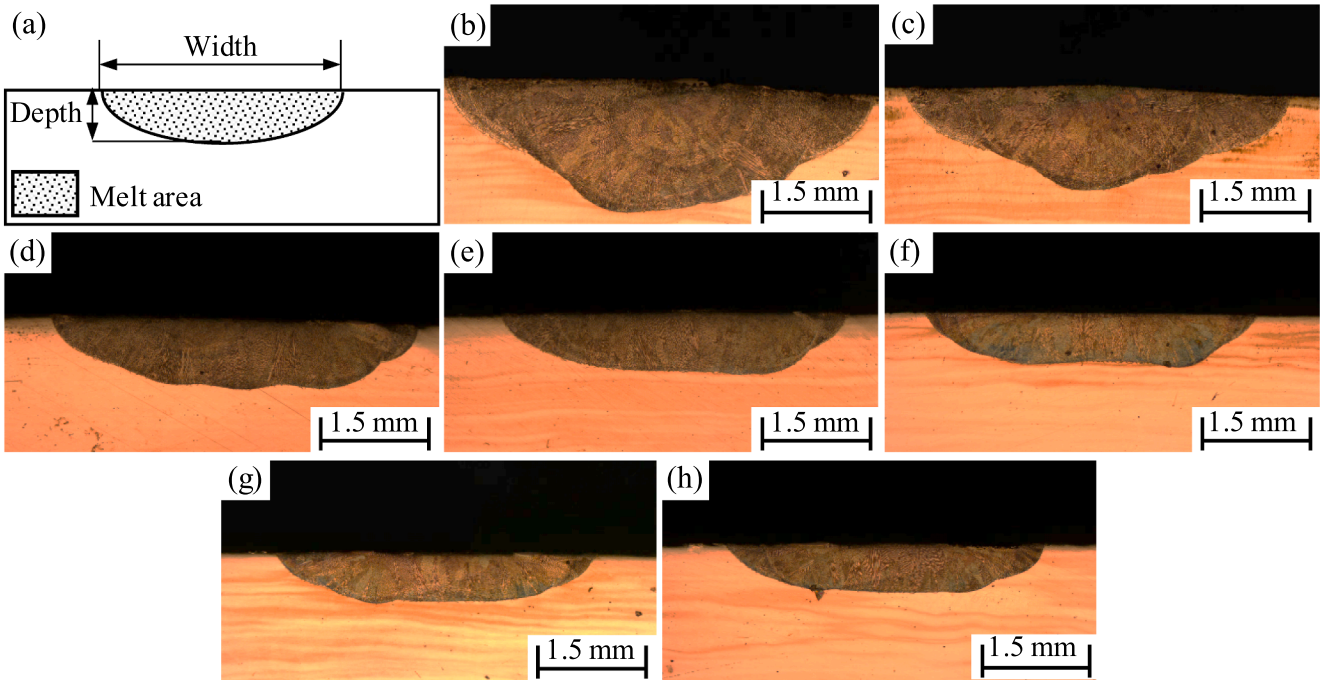

Fig. 10. Evolution of melt geometry (cross-section) with increase in the laser scan speed (a) geometry considered, (b) 200 mm/min, (c) 400 mm/min, (d) 600 mm/min, (e) 800 mm/min, (f) 1000 mm/min, (g) 1200 mm/min and (h) 1400 mm/min (1200 W, 3 mm spot diameter).

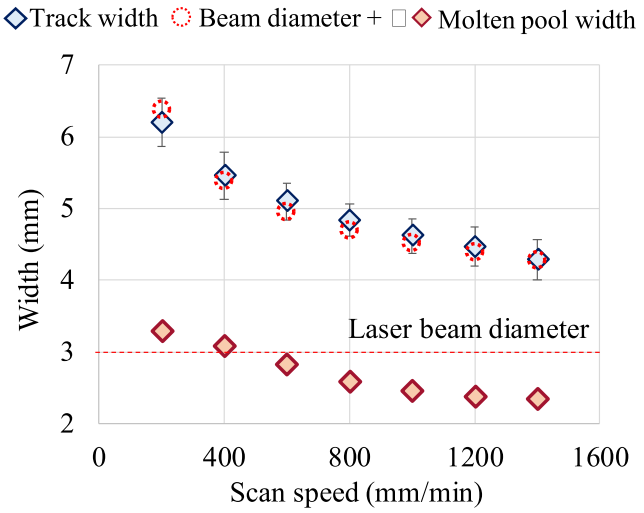

Fig. 12. Correlation between the width of the remelted track, the molten pool width (recorded using a camera), and the beam diameter plus thermal diffusion length (δ) (1200 W, 3 mm spot diameter).

reported by Long [17] and they closely correlate with the values given in Zhao et al. [18] and You et al. [19]. However, the estimated values differ significantly from the results of Shi et al. [20], which is due to the intrinsic nature of the processes being compared, i.e., an extremely slow cooling process [20] against a fast cooling laser process. From the above results, it can be observed that the cooling rates measured experimentally could be used for predicting the microstructure evolution in the laser remelting process without the need for post-processing of the samples, i.e., sectioning and SEM analysis.

3.2. Influence of laser scan speed on melt geometry

Figs. 10 and 11 show the cross-section of the remelted tracks and their variation with respect to laser scan speed, respectively. Since the scan speed is reported to have a significant effect on the cooling rate [6], in the current study, keeping the laser beam power constant, the scan speed is varied. From Figs. 10 and 11, it can be observed that the melt pool width, depth, and area show a decreasing trend with an increase in the laser scan speed. This is due to the decrease in line energy with an increase in scan speed [21], as discussed in section 3.1. Irrespective of the laser scan speed, it can be observed from Figs. 10 and 11 that in all the cases, the melt width is higher than the selected laser spot diameter (3 mm). This is attributed to the lateral conduction of heat from the molten pool. Within the experimental range of the present study, it may be observed that the thermal diffusion length δ (defined in Eq. 1) is comparable to that of the spot diameter, indicating a lateral conduction phenomenon [22]. Fig. 12 shows the correlation between the melt width, laser beam diameter, and thermal diffusion length. It can be observed that in all the cases, the melt width is approximately equal to the sum of the laser beam diameter and the thermal diffusion length.

Similar to the melt width, the melt depth is also found to decrease with an increase in scan speed. It may be interesting to note that, in the case of scan speed ranging from 1200 mm/min to 600 mm/min, the remelt depth is found to be uniform along the width. Whereas, in the case of 400 mm/min and 200 mm/min, the depth varies along the width with the maximum being at the center.

This could be due to the near Gaussian intensity profile of the laser beam (Fig. 1(b)), which, with increased interaction time ($\frac{Laser\ spot\ diameter}{Scan\ speed}$) and line energy, results in the onset of vaporization from the molten pool center, forming a keyhole [23,24], thus increasing the laser absorption and the melt depth at the molten pool center.

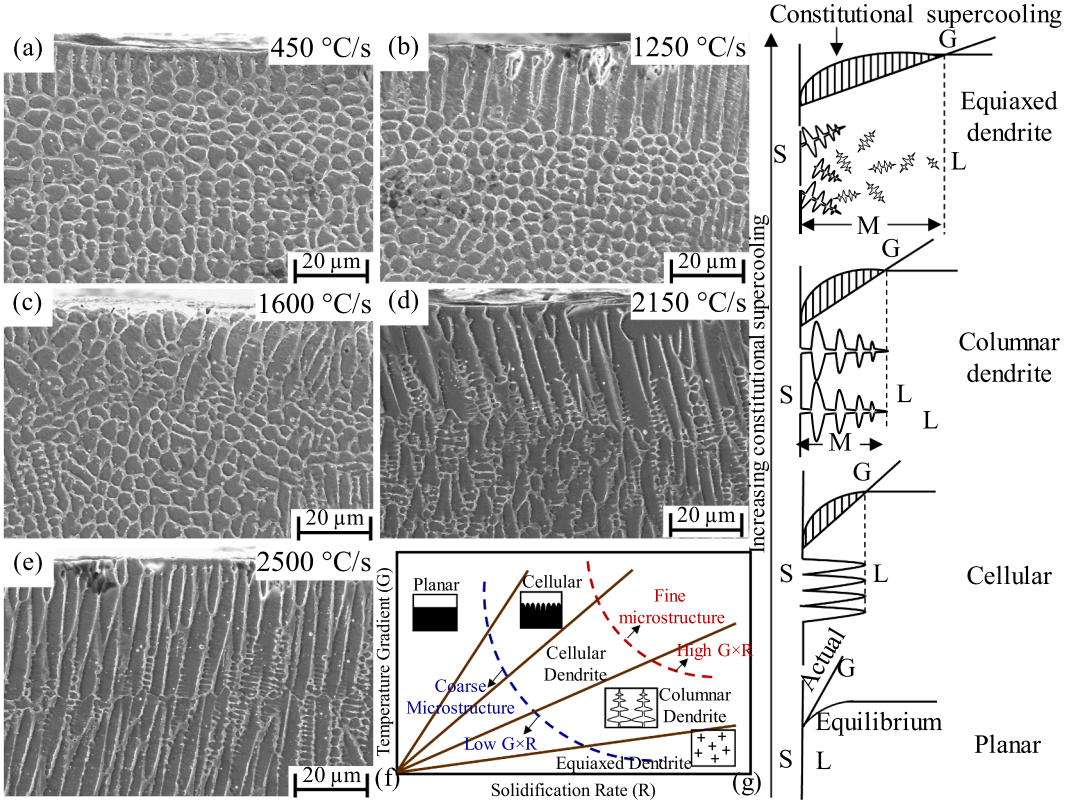

Fig. 13. Effect of (a) - (e) scan speed on evolution of microstructure (a) 200 mm/min, (b) 600 mm/min, (c) 800 mm/min, (d) 1000 mm/min, (e) 1200 mm/min. (1200 W, 3 mm spot diameter) (f) *G* and *R* on the solidification morphology [25] and (g) mode of solidification with respect to temperature gradients (*G*) and constitutional supercooling.

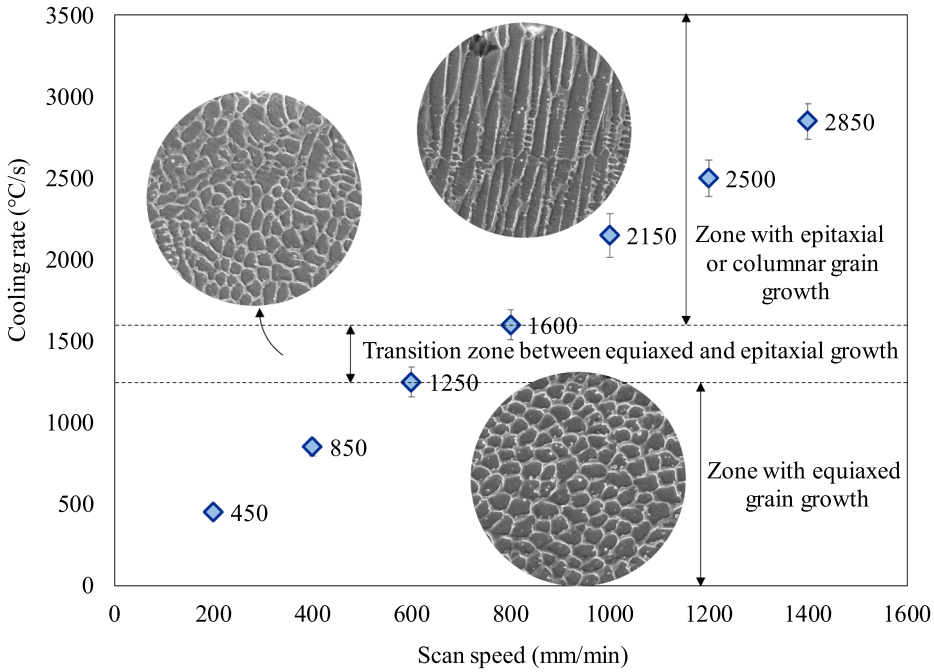

Fig. 14. Correlation between cooling rate and evolution of microstructure.

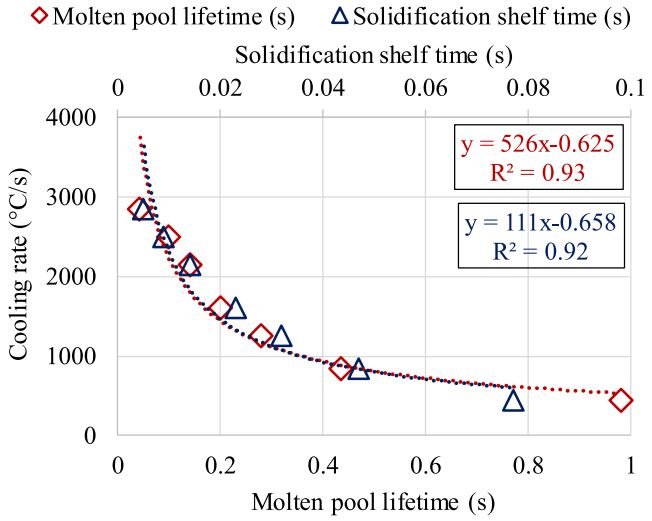

Fig. 15. Correlation between cooling rate, molten pool lifetime, and solidification shelf time.

3.3. Correlation between process parameters, cooling rate, and microstructure evolution

Fig. 13 (a)–(e) shows the effect of scan speed, varied in the range of 200 mm/min to 1200 mm/min, on the microstructure evolution during laser surface remelting of Inconel 718. From Fig. 13 (a) and (b), it is observed that at lower scan speeds of 200 mm/min and 600 mm/min, the microstructure consists of equiaxed or stray grains near the surface of the remelted sample. In the case of 600 mm/min, a slight columnar dendritic structure is observed at the surface. As discussed in the experimental details, Argon gas at 10 l/min flow rate is used as the shielding gas which directly interacts with the surface of molten pool resulting in a forced convection increasing its cooling rate leading to a thin layer formation with columnar structure [4]. Further, it can be observed that equiaxed grains in case of 600 mm/min are refined/fine compared to 200 mm/min. This is due to the faster cooling rate in case of 600 mm/min, i.e., 1250 °C/s, compared to 450 °C/s in case of 200 mm/min. As discussed in Fig. 4, at a lower scan speed, i.e., 400 mm/min, the molten pool stays at a high temperature (above 1335 °C) for a longer duration and cools down slowly to 600 °C as compared to a scan speed of 1200 mm/min. This is due to the increased line energy and interaction time with a decrease in the scan speed, resulting in larger molten pool size and a reduced temperature gradient due to the heat conduction. Further, this reduction in temperature gradient and longer interaction time also results in the thermalization of the molten pool i.e., temperature difference within the molten pool from solid-liquid interface to the molten pool surface reduces.

This, in turn, results in a decrease in the temperature gradient (G) within the molten pool, converting it into a mushy region (M) resulting in higher solidification velocity (R) with constitutional supercooling, forming nucleation sites across the molten pool, leading to equiaxed dendritic structure as depicted in Fig. 13 (f) and (g) [25]. In the case of 800 mm/min scan speed corresponding to 1600 °C/s cooling rate, the microstructure consists of both equiaxed and cellular dendritic structures. With further increase in scan speed to 1000 mm/min and 1200 mm/min, the microstructure became fully cellular in nature, with some misorientation arising in the case of 1000 mm/min due to the relatively slow cooling rate as compared to 1200 mm/min, which is found to be 2150 °C/s and 2500 °C/s respectively. At a higher scan speed, due to the lower interaction time, the temperature gradient along the depth of the molten pool is expected to be high, resulting in a columnar/cellular microstructure as shown in Fig. 13 (d) and (e), and further depicted in Fig. 13 (f) and (g).

Based on the above observations, a process map is established as a function of the cooling rate, as shown in Fig. 14. One can observe that a cooling rate below 1250 °C/s results in equiaxed grains, while above 1600 °C/s would result in cellular/columnar microstructure. Between these two zones, there exists a transition zone, as represented in Fig. 14, where a combination of both the microstructures co-exists. It may be noted that the dependence of morphology is usually correlated with G/R and feature size with $G \times R$, i.e., the cooling rate. However, in the present study, the cooling rate is used to correlate the morphology as the determination of the solidification velocity (R) in the case of opaque material in real-time is quite difficult. Further, from Fig. 15, it may be observed that there exists a good correlation between cooling rate and

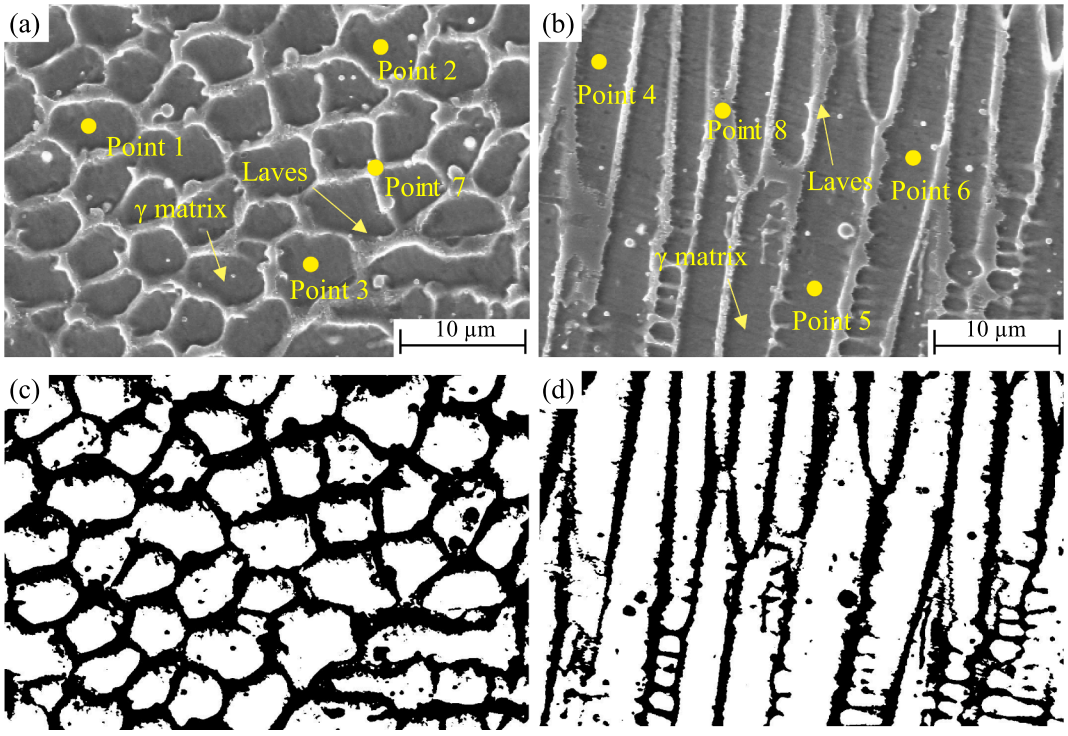

Fig. 16. Effect of scan speed on microstructure and laves phase percentage (a), (c) 200 mm/min and (b), (d) 1400 mm/min (1200 W, 3 mm spot diameter).

Table 3
Elemental composition (wt%) of γ-matrix obtained from EDS analysis.

Location	Elements Wt%						
	Ni	Cr	Fe	Nb	Mo	Ti	Al
Point 1	56.99	21.25	19.56	1.25	0.81	0.12	0.02
Point 2	56.21	22.67	18.96	1.42	0.65	0.08	0.01
Point 3	58.31	20.81	18.95	0.86	0.92	0.13	0.02
Average of point 1,2 and 3	57.17	21.58	19.16	1.18	0.79	0.11	0.02
Point 4	55.81	19.36	20.1	2.25	1.59	0.86	0.03
Point 5	57.32	19.38	19.26	2.01	1.06	0.95	0.02
Point 6	56.12	18.86	20.2	1.92	1.97	0.88	0.05
Average of point 1,2 and 3	56.42	19.20	19.85	2.06	1.54	0.90	0.03
Point 7	47.14	15.81	14.16	17.43	3.61	1.77	0.08
Point 8	50.04	16.10	14.38	14.18	3.03	2.21	0.06

molten pool lifetime or solidification shelf time which are directly related to the solidification velocity. Process maps of this nature, where structural evolution is correlated with the cooling rate would help us to evaluate the control limits for developing feedback control systems in laser material processing like surface remelting, additive manufacturing, welding, etc., to improve reproducibility and repeatability [26].

3.4. Effect of cooling rate and microstructure on wear properties

In section 3.3, it has been observed that with a decrease in cooling rate, changes in both the grain structure as well as coarsening of grains occurred. Further, in Nickel-based super alloys like Inconel 718, elemental segregation is one of the major issues, being a precipitation strengthened nickel-based superalloy containing Nb, Ti, and Al as alloying elements. During the solidification process, the alloying elements are expected to form γ' and γ'' phases (intermetallic phases), γ' is based on $Ni_3(Al, Ti)$, which has an ordered FCC L12 structure, while γ'' is based on Ni_3Nb, which has a body-centered tetragonal DO22 structure. Both the phases are coherent with the γ-Ni solid-solution matrix, i.e., Ni-Cr-Fe.

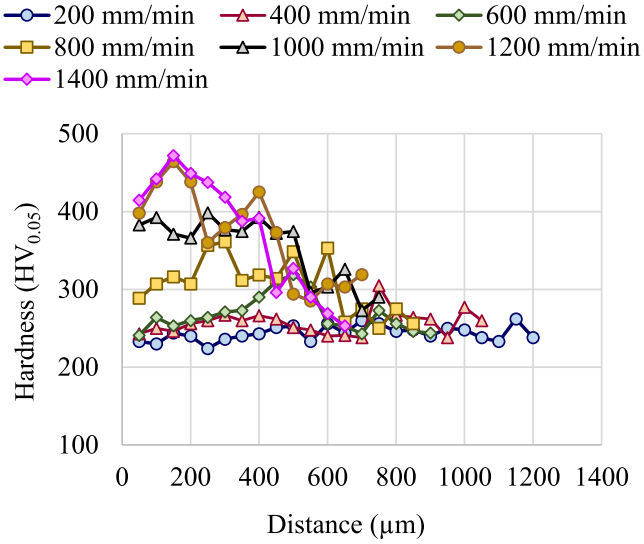

Fig. 17. Effect of scan speed on the hardness values (1200 W, 3 mm spot diameter).

The main principle of the strengthening mechanism involved is the anti-phase boundary hardening arising from the coherent and ordered γ' and γ'' phases [27,28]. However, during the solidification process, the precipitation strengthening elements are susceptible to segregation owing to their low equilibrium distribution coefficients k, which is defined as $k = C_S/C_L$, where C_S and C_L are the compositions of solid and liquid at the solid–liquid interface [29]. However, it may be worth noting that rapid solidification can entrap the alloying elements in the γ matrix, which in turn can prevent or reduce the CET or equiaxed grain layer thickness, as well as reduce the elemental segregation or formation of Laves phase, which are brittle in nature [6]. Fig. 16 shows the SEM

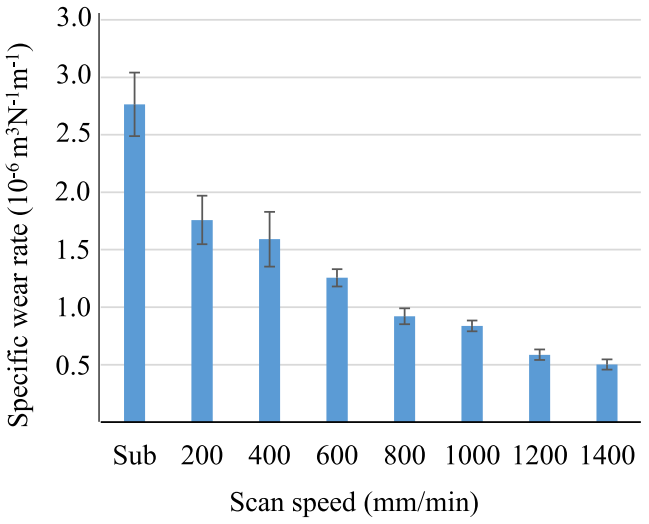

Fig. 18. Effect of scan speed on the specific wear rate (1200 W, 3 mm spot diameter).

images depicting the microstructure near the surface in case of 200 mm/min and 1400 mm/min scan speed. The Laves phase percentage at the grain boundary is estimated using ImageJ open-source software, where the volume fraction is identified using Fig. 16 (c) and (d) by performing an image thresholding operation to generate binary images. Laves phase percentage in the case of 200 mm/min is around 43 %, while in the case of 1400 mm/min, it is close to ~29 %.

Further, EDS analysis is also carried out in the dendritic core region or inside the grains and on Laves phase at different locations, as shown in Fig. 16(a) and (b). Based on the EDS results presented in Table 3, the weight% of phase strengthening alloying elements inside the grains, i.e., Nb, Mo, Ti, and Al, is less in the case of 200 mm/min as compared to the 1400 mm/min case. Therefore, faster cooling rates not only favor the formation of columnar structure but also help in reducing the elemental segregations by entrapping the alloying elements inside the γ-matrix. Further, as shown in the Table 3, it may observed that the weight percentage of Nb, Mo and Ti at the grain boundary or Laves phase is high compared to the γ matrix.

To study the effect of the cooling rate and the corresponding structure and resulting elemental segregation on the mechanical properties, a hardness and wear test is also carried out. Fig. 17 shows the variation in hardness along the depth of the remelted surface obtained at various scan speeds. It is observed that in the case of scan speeds between 200 mm/min to 600 mm/min, the hardness value is close to that of the substrate (256 $\pm$ 12 $HV_{0.05}$), while in the case of 800 mm/min and above, the hardness level showed an increasing trend. From Figs. 13 and 14, it may be observed that scan speeds between 200 mm/min and 600 mm/min resulted in equiaxed grains, whereas scan speeds above 800 mm/min resulted in columnar structure. Further, it may be noted that the columnar structure gets refined with an increase in cooling rate, as evident from Figs. 8 and 13. It can also be observed from Fig. 16 and Table 3 that a faster cooling rate resulted in the entrapment of alloying elements in the dendritic core, minimizing the elemental segregation or formation of Laves phase. Therefore, the increase in hardness level with the cooling rate or the scan speed may be attributed to grain refinement as well as reduced elemental segregation.

Fig. 18 shows the variation in specific wear rate with scan speed. It can be observed that with an increase in scan speed, the specific wear rate gets reduced. This may be attributed to the grain refinement because of increased cooling rate and reduced elemental segregation. Further, the wear surface and debris are analyzed using an SEM to ascertain the mode of wear. From Fig. 19, it can be observed that the samples remelted at higher scan speeds showed ploughing as a significant wear mechanism. In the case of lower scan speeds, i.e., 400 mm/min and 200 mm/min, micro-cracking and delamination are found to be the major wear mechanism, as depicted in Fig. 19(c) and (d).

Further, from the wear debris analysis presented in Fig. 20, one can observe that at lower scan speeds, the debris size is larger. As discussed in previous sections, the slower cooling rates result in the formation of more Laves phases which are brittle in nature [6], resulting in the formation of micro-cracks and delamination during the wear process. Therefore, slower scan speeds or cooling rates will result in poor surface

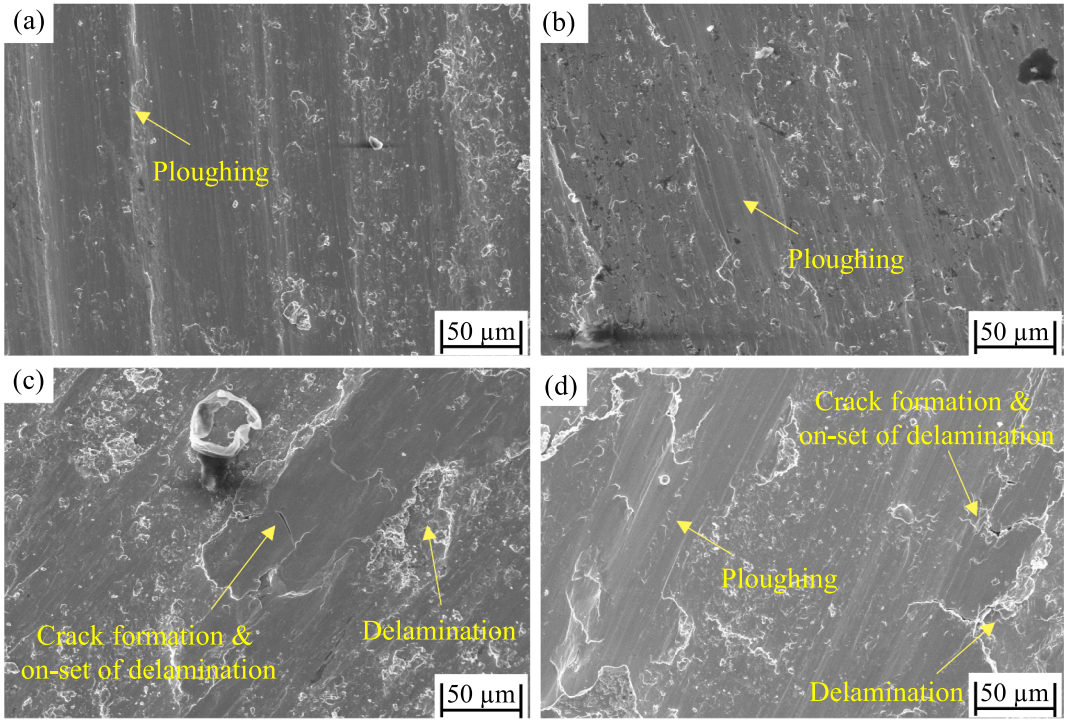

Fig. 19. Wear surface morphology (a) 1400 mm/min, (b) 1200 mm/min, (c) 400 mm/min, (d) 200 mm/min (1200 W, 3 mm spot diameter).

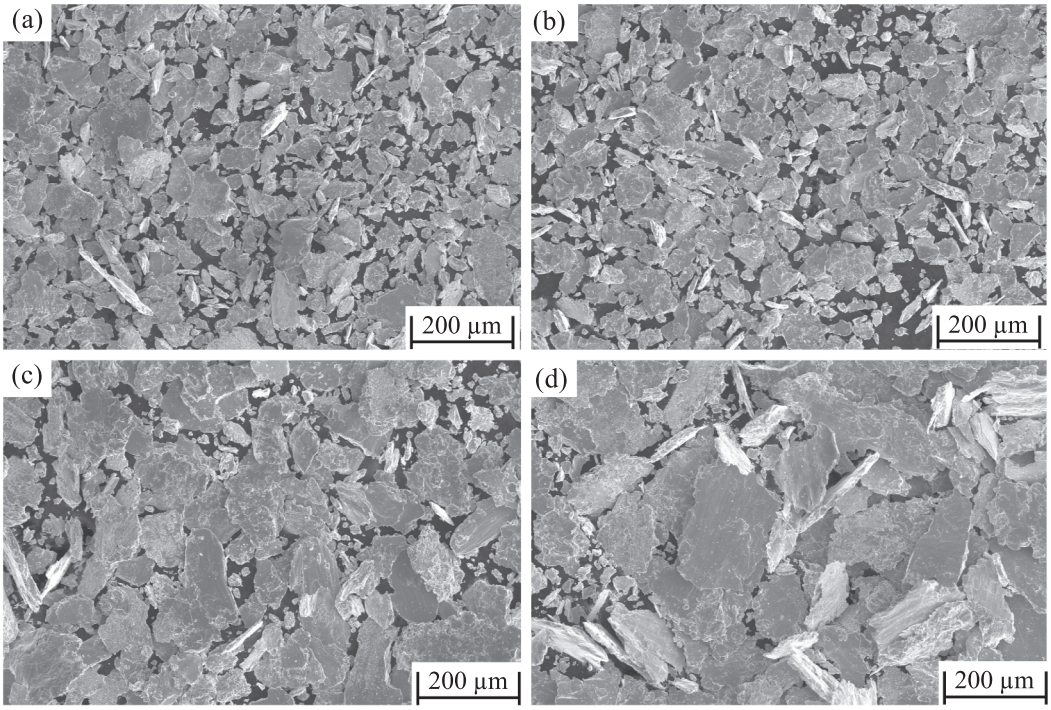

Fig. 20. Wear debris morphology (a) 1400 mm/min, (b) 1200 mm/min, (c) 400 mm/min, (d) 200 mm/min (1200 W, 3 mm spot diameter).

properties compared to higher cooling rates.

4. Conclusion

Laser surface remelting is a surface engineering technique used to modify the surface properties, without affecting the bulk properties of the material. However, the extent of improvement in the surface properties depends on the thermal cycle experienced by the surface during the remelting process. In order to quantify these effects, the molten pool thermal history during the laser surface remelting of Inconel 718 has been monitored using an IR pyrometer, and a correlation between the evolution of microstructure, scan speed, cooling rate and, mechanical properties is established. Further, a process map correlating the evolution of microstructure with cooling rate has been developed. Based on the experimental observations, the following conclusions can be drawn:

(a) With the increase in laser scan speed, remelt width, depth, and area decrease.
(b) Cooling rate increases with an increase in scan speed.
(c) A process map correlating cooling rate and evolution of microstructure for laser surface remelting of Inconel 718 has been developed. A cooling rate below 1250 °C/s results in an equiaxed grain structure, while above 1600 °C/s results in columnar/cellular microstructure.
(d) Faster cooling rates result in entrapment of alloying elements in the dendritic structure, while slower cooling rates result in increased volume fraction of Laves phase.
(e) Faster cooling rates result in increased surface hardness and specific wear rate due to grain refinement and entrapment of alloying elements in the dendritic core.

Declaration of Competing Interest

The authors declare that they have no known competing financial interests or personal relationships that could have appeared to influence the work reported in this paper.

Data availability

Data will be made available on request.

Acknowledgment

The financial support from the Science and Engineering Research Board (SERB) under the startup research grant program (SRG/2019/000153) is gratefully acknowledged. The authors also gratefully thank the Department of Mechanical Engineering, IIT Kharagpur, for extending the facilities which are financially supported by the Department of Science and Technology, Government of India, under the FIST Program-2007 (SR/FIST/ETII-031/2007), and the Ministry of Human Resource Development and Department of Heavy Industries, Government of India, under the IMPRINT Program-2017 for Project-6917.

References

[1] N. Eliaz, G. Shemesh, R.M. Latanision, Hot corrosion in gas turbine component, Eng. Fail. Anal. 9 (2002) 31–43.
[2] M. Cemal, S. Cevik, Y. Uzunonat, F. Diltemiz, ALLVAC 718 PlusTM Superalloy for Aircraft Engine Applications. In: Agarwal R, editor. Recent Adv. Aircr. Technol., vol. 718, Eskisehir, Turkey: InTech, 2012, pp. 75–96.
[3] S.G.K. Manikandan, D. Sivakumar, M. Kamaraj, Welding the Inconel 718 Superalloy: Reduction of Micro-segregation and Laves Phases, Elsevier, 2019, xiii–xvi, ISBN 9780128181829.
[4] Z. Lei, N. Lu, X. Yu, Epitaxy and new stray grain formation mechanism during epitaxial laser melting deposition of Inconel 718 on directionally solidified nickel-based superalloys, J. Manuf. Processes 42 (2019) 11–19.
[5] W. Kurz, D.J. Fisher, Fundamentals of Solidification, 4th revised ed., Trans Tech Publications Ltd, Switzerland, 1998.
[6] M. Gopinath, D.P. Karmakar, A.K. Nath, Online monitoring of thermo-cycles and its correlation with microstructure in laser cladding of nickel based super alloy, Opt. Lasers Eng. 88 (2017) 139–152.
[7] R. Koike, T. Misawa, T. Aoyama, M. Kondo, Controlling metal structure with remelting process in direct energy deposition of Inconel 625, Manuf. Technol. 67 (2018) 237–240.
[8] S.K. Sharma, K. Biswas, A.K. Nath, I. Manna, J. Dutta Majumdar, Microstructural change during laser welding of Inconel 718, Optik 218 (2020) 165029.
[9] S.K. Sharma, K. Biswas, J. Dutta Majumdar, Wear behaviour of Electron beam surface melted Inconel 718, Proc. Manuf. 35 (2019) 866–873.

[10] Y. Liang, H. Wang, Origin of stray-grain formation and epitaxy loss at substrate during laser surface remelting of single-crystal nickel-base superalloys, Mater. Des. 102 (2016) 297–302.
[11] H. Helmer, A. Bauereiß, R.F. Singer, C. Körner, Grain structure evolution in Inconel 718 during selective electron beam melting, Mater. Sci. Eng., A 668 (2016) 180–187.
[12] Y. Zhang, Z. Li, P. Nie, Y. Wu, Effect of cooling rate on the microstructure of laser-remelted INCONEL 718 coating, Metall. Mater. Trans. A 44A (2013) 5513–5521.
[13] Y.K. Madhukar, S. Mullick, D.K. Shukla, S. Kumar, A.K. Nath, Effect of laser operating mode in paint removal with a fiber laser, Appl. Surf. Sci. 264 (2013) 892–901.
[14] G. Muvvala, D. Patra Karmakar, A.K. Nath, Online assessment of TiC decomposition in laser cladding of metal matrix composite coating, Mater. Des. 121 (2017) 310–320.
[15] T. Antonsson, H. Fredriksson, The effect of cooling rate on the solidification of INCONEL 718, Metall. Mater. Trans. B 36 (1) (2005) 85–96.
[16] L. Zhao, Y.i. Tan, S. Shi, X. You, P. Li, C. Cui, Microsegregation behavior of Inconel 718 superalloy prepared by electron beam smelting layered solidification technology, J. Alloy. Compd. 833 (2020) 155019.
[17] Y.-T. Long, P.-L. Nie, Z.-G. Li, J. Huang, X. Li, X.-M. Xu, Xu, Segregation of niobium in laser cladding Inconel 718 superalloy, Trans. Nonferrous Metals Soc. China 26 (2) (2016) 431–436.
[18] J. Zhao, P. Yan, The effect of cooling rate of solidification on microstructure and alloy element segregation of as cast alloy 718, in: E.A. Loria (Ed.), Superalloys 718, 625,706 Var, TMS, Deriv., 2001, pp. 133–140.
[19] X. You, Y. Tan, S. Shi, J.-M. Yang, Y. Wang, J. Li, Q. You, Effect of solution heat treatment on the precipitation behavior and strengthening mechanisms of electron beam smelted Inconel 718 superalloy, Mater. Sci. Eng., A 689 (2017) 257–268.
[20] X. Shi, S.-C. Duan, W.-S. Yang, H.-J. Guo, J. Guo, Effect of cooling rate on microsegregation during solidification of superalloy INCONEL 718 under slow cooled conditions, Metall. Mater. Trans. B 49 (4) (2018) 1883–1897.
[21] S.S. Chakraborty, S. Dutta, Estimation of dilution in laser cladding based on energy balance approach using regression analysis, Sādhanā 44 (150) (2019) 1–6.
[22] W.M. Steen, J. Mazumder (Eds.), Laser Material Processing, Springer London, London, 2010.
[23] S. Im, S. Jun, J. Lee, J. Lee, B. Lee, H. Lee, H. Hong, Unidirectional columnar microstructure and its effect on the enhanced creep resistance of selective electron beam melted Inconel 718, J. Alloy. Compd. 817 (2020) 153320.
[24] Q. Jia, D. Gu, Selective laser melting additive manufacturing of Inconel 718 superalloy parts: densification, microstructure and properties, J. Alloy. Compd. 585 (2014) 713–721.
[25] S. Kou, Welding Metallurgy, second ed., John Wiley & Sons Inc, Hoboken, 2002.
[26] A.M. Nair, G. Muvvala, S. Sarkar, A.K. Nath, Real-time detection of cooling rate using pyrometers in tandem in laser material processing and directed energy deposition, Mater. Lett. 277 (2020) 128330.
[27] C.T. Sims, N.S. Stoloff, W.C. Hagel, Superalloys II, John Wiley & Sons, New York, 1987.
[28] J.M. Oblak, D.F. Paulonis, D.S. Duvall, Coherency strengthening in Ni base alloys hardened by DO22 γ'' precipitates, Metallurgical, Transactions 5 (1974) 143–153.
[29] A. Odabasi, N. Unlu, G. Goller, M.N. Eruslu, A study on laser beam welding (LBW) technique: effect of heat input on the microstructural evolution of superalloy Inconel 718, Metall. Mater. Trans. A 41 (2010) 2357–2365.